

Article

Characteristics and Formation Conditions of Se-Bearing Metacinnabar in the Wanshan Mercury Ore Field, Eastern Guizhou

Xiao Wang ^{1,2}, Jiajun Liu ^{1,2,*} , Emmanuel John M. Carranza ³, Degao Zhai ^{1,2}, Qingqing Zhao ^{1,2}, Guoming Weng ^{1,2} and Bin Zhang ^{1,2}

- ¹ State Key Laboratory of Geological Processes and Mineral Resources, China University of Geosciences (Beijing), Beijing 100083, China
² School of Earth Sciences and Resources, China University of Geosciences (Beijing), Beijing 100083, China
³ Department of Geology, University of the Free State, Bloemfontein 9301, South Africa
* Correspondence: liujiajun@cugb.edu.cn; Tel.: +86-010-82321856

Abstract: Cinnabar (α -HgS) is the most common sulfide of mercury while metacinnabar (β -HgS), a high-temperature homogeneous polymorph of the mercury sulfide, is relatively rare, and the α phase of cinnabar transforms to the β phase at 344 °C. Meanwhile, there is a complete isomorphic series between HgS and HgSe, and the occurrence of Se-bearing metacinnabar is of great significance for the exploration of selenium resources. We studied through microscopic observation, electron-probe microanalysis, X-ray diffraction and field emission scanning electronic microscopy (FESEM) the Se-bearing metacinnabar of the Wanshan mercury ore field of southeastern Yangtze Block. These analyses, combined with physicochemical phase diagrams, constrained the textural and chemical evolution during the formation process of Se-bearing metacinnabar. Se-bearing metacinnabar was found in altered carbonatite, intergrown with cinnabar, sphalerite, pyrite, realgar and quartz. The Se-bearing metacinnabar contains 77.66–84.01 wt.% Hg, 0.18–1.17 wt.% Zn with extensive isomorphic substitution of Se and S (2.79–14.77 wt.% Se, 6.15–11.82 wt.% S). The presence of impurity elements (e.g., Zn and Se) is considered to be the key factor in expanding the stable range of Se-bearing metacinnabar. The cinnabar generated by the transformation of Se-bearing metacinnabar is characterized by inclusions of Hg-bearing sphalerite and pores, which indicate that this process was carried out through a coupled dissolution–reprecipitation (CDR) reaction. The formation temperature of Se-bearing metacinnabar is higher than that of cinnabar, and according to the phase relations between sulfides and selenides, we propose that $\log f_{S_2}(g)$ of ore-forming fluids is constrained within -15.663 to -13.141 , and $\log f_{Se_2} < \log f_{S_2} - 3.994$ (150 °C).

Keywords: cinnabar; coupled dissolution–reprecipitation reactions; polymorphic phase transformations; selenium-bearing metacinnabar; Wanshan mercury ore field; Eastern Guizhou



Citation: Wang, X.; Liu, J.; Carranza, E.J.M.; Zhai, D.; Zhao, Q.; Weng, G.; Zhang, B. Characteristics and Formation Conditions of Se-Bearing Metacinnabar in the Wanshan Mercury Ore Field, Eastern Guizhou. *Minerals* **2023**, *13*, 173. <https://doi.org/10.3390/min13020173>

Academic Editor: Dimitrina Dimitrova

Received: 26 November 2022

Revised: 19 January 2023

Accepted: 23 January 2023

Published: 25 January 2023



Copyright: © 2023 by the authors. Licensee MDPI, Basel, Switzerland. This article is an open access article distributed under the terms and conditions of the Creative Commons Attribution (CC BY) license (<https://creativecommons.org/licenses/by/4.0/>).

1. Introduction

Cinnabar (α -HgS), the most common sulfide of mercury, has a hexagonal structure (space group $P3_121$), while its high-temperature homogeneous multiphase variant metacinnabar (β -HgS) is rare and has a cubic structure (space group $F43m$) [1,2]. Metacinnabar and tiemannite are the two end-member minerals of the HgS–HgSe homogeneous series, the former being a S-rich end-member and the latter a Se-rich end-member [3,4]. Dickson [5] reported that metacinnabar is in a metastable state at room temperature, and experiments have shown that β -HgS (metacinnabar) will change rapidly to α -HgS (cinnabar) when the temperature is cooled below 344 ± 2 °C. Some studies also suggested that cinnabar and metacinnabar crystals can coexist in equilibrium under a temperature range of 345–315 °C in the Hg–S system [6,7]. However, the addition of impurity elements such as Fe, Zn, and Se enlarges the phase transition temperature between α -HgS

(cinnabar) and β -HgS (metacinnabar), expanding the stable range of metacinnabar [8–10]. At present, metacinnabar (β -HgS) with Zn, Se, Fe or Mn admixtures are considered as equivalent varieties of metacinnabar (e.g., zincian metacinnabar; Se-bearing metacinnabar, etc.) [11].

Se-bearing metacinnabar has been found in the Xiangxi (western Hunan)–Qiandong (eastern Guizhou) Hg Mineralization Belt in recent years (Table 1). Previous electron-probe microanalyses show that some metacinnabar with high Se content may contain independent minerals of Se [12]. Thus, a study on the formation of Se-bearing metacinnabar is of great significance for the exploration of Se resources. Liu [13] considered that Se-bearing metacinnabar is formed under the conditions of an insufficient S component of the ore-forming fluid (low fS_2) or high oxygen fugacity (fO_2), and high fSe_2 values, and fSe_2/fS_2 ratios are the key factors controlling the precipitation of Se-bearing metacinnabar [14]. As metacinnabar is a high-temperature variant of cinnabar, and the admixture of impurity elements has an important influence on the stable existence of metacinnabar, it is not sufficient to discuss the causes of the formation of metacinnabar containing Se in terms of fS_2 and fSe_2 alone. In this paper, the textural and chemical evolution during the formation of Se-bearing metacinnabar in the Wanshan mercury ore field are discussed based on mineral assemblages, microscopic observation, field emission scanning electronic microscopy (FESEM) as well as X-ray diffraction (XRD) and electron-probe microanalysis (EPMA).

Table 1. Chemical compositions of metacinnabar from some mercury deposits (wt.%).

No.	Hg	Fe	Zn	Cd	Se	S	Total	Ore Occurrence Deposit	Reference
1	85.54	0.04				12.67	98.25	Zhifang, Guizhou, China	Chen [15]
	85.58	0.06				12.41	98.05		
2	84.06	0.01			2.00	12.51	98.58	Dadongla, Guizhou, China	Chen [15]
	82.67	1.07			1.00	14.80	99.54		
3	77.96	0.06	5.70			14.92	98.64	Chatian, Guizhou, China	Chen [15]
	76.57		6.13			15.50	98.2		
	77.24	0.04	6.57			14.96	98.81		
4					4.64			Zhifang, Guizhou, China	Zeng [16]
5	83.64				6.52		90.16	Jiudiantang, Hunan, China	Bao [17]
6	84.04				4.23	11.02	99.29	Baojing, Hunan, China	Huang [14]
7	77.42		0.02		19.04	4.20	100.68	Dongping, Hunan, China	Liu [13]
	76.88	0.01			15.25	6.35	98.49		
	76.81		0.07		17.60	4.14	98.62		
	80.18	0.02	0.17		14.63	6.44	101.44		
	78.92	0.05	0.05		14.66	6.62	100.3		
	78.58	0.02			13.24	7.20	99.04		
	78.30	0.01	0.19		14.69	6.58	99.77		
	78.43	0.02	0.09	0.02	15.26	6.32	100.14		
	79.33	0.04	0.04		14.64	6.71	100.76		
	78.37		0.05	0.04	13.76	7.04	99.26		
	80.31	0.02	0.19		13.29	7.19	101		
	77.95	0.02	0.05		14.86	6.47	99.35		
	79.38	0.03	0.13		13.54	7.16	100.24		
	79.18	0.02	0.19	0.01	13.87	6.81	100.08		
	79.73				13.91	6.64	100.28		
	80.1	0.02	0.13	0.01	13.24	7.13	100.63		
	81.34	0.03	1.08	0.05	8.59	9.28	100.37		
83.97		0.59	0.01	6.81	10.32	101.7			
77.2	0.02	0.22		19.21	4.34	100.99			
81.13				11.07	8.01	100.21			
80.75	0.06	0.61	0.04	10.30	8.33	100.09			
79.65	0.01	0.25		13.18	6.89	99.98			

Table 1. Cont.

No.	Hg	Fe	Zn	Cd	Se	S	Total	Ore Occurrence Deposit	Reference
	79.65	0.04	0.26	0.06	11.22	7.98	99.21		
	77.76	0.02	0.08		13.95	6.58	98.39		
	80.95	0.03	0.23	0.03	10.4	8.69	100.33		
	81	0.06	0.6	0.02	8.91	9.34	99.93		
	76.57	0.01	0.04		18.39	4.65	99.66		
	78.92		0.13		16.35	5.47	100.87		
8	79.05		4.8	1.07		15.51	100.43	Chauvai, Kyrgyzstan	Vasil'ev [11]
	79.3		4.46	0.75		15.29	99.8		
	78.95		4.31	1.27		15.29	99.82		
9	56.43		10.35	13.98	0.26	17.8	98.82	Murzinskoe	Vasil'ev [11]
	56.47		10.7	14.1	0.27	18.19	99.73		
	56.25		10.83	14.1	0.19	18.3	99.67		
	56.42		10.24	13.74	0.3	18.04	98.74		
	55.47		10.51	13.35	0.24	18.36	97.93		
10 *	77.68	5.36				14.97	98.01	Felsöbánya, Transylvania	Dickson [5]
11 *	79.73		4.23		1.08	14.58	99.62	Guadalcazar, Mexico	Dickson [5]
12 *	79.69	1.04	3.32			14.97	99.02	Pola de Lena, Spain	Dickson [5]
13 *	83.38		2.17			14.24	99.79	Levigliani, Italy	Dickson [5]
14 *	81.83				6.49	10.3	98.62	San Onofre, Mexico	Dickson [5]
15	80.95	0.44	1.82		0.22	15.99	99.42	Levigliani, Italy	Din [18]
	82.06	0.3	2.13		0.12	16.13	100.74		
16	83.61	1.88	0.07			14.03	99.59	Diablo Mountain, CA, USA	Boctor [19]
	83.14	2.15				14.34	99.63		
	84.67	0.96	0.15			14.29	100.07		
	82.98	2.49	0.15			14.52	100.14		
	82.12	0.13	0.23		6.15	10.18	98.81		
	83.28	0.27	0.29		4.05	11.88	99.77		
	84.28	0.38	0.25		2.91	12.11	99.93		
	84.45	0.74	0.1		1.17	12.96	99.42		
	85.39	0.66	0.2		0.5	13.81	100.56		

Note: 1–9, 15–16, microprobe analyses; *, test method unknown.

2. Regional Geology

The Xiangxi (western Hunan)–Qiandong (eastern Guizhou) Hg Mineralization Belt, also called the Tongren–Fenghuang Hg Mineralization Belt (TFHB), is situated in the north-eastern sector of the Xiangxi (western Hunan)–Qiandong (eastern Guizhou) Pb–Zn–Hg metallogenic belt (Figure 1a), along the southeastern margin of the Yangtze Block [20]. The TFHB is 150 km long and 5–10 km wide, with a series of deposits distributed along a NW–SW trend. To date, about 72 Hg-bearing deposits (accounting for 50% of the existing Hg reserves in China) have been found in the TFHB, which hosts several super-large to medium-scale Hg deposits, making it the most important mercury resource base in China [21,22]. It is important to note that most of the Hg deposits are very rich in Se and Se minerals. For example, the cinnabar in the Kezhai Hg deposit of the Wanshan ore field contains considerable Se with an average content of 663 ppm [23]; the metacinnabar in the Dongping Hg–Ag–Se deposit contains 6.81–19.21 wt.% Se [13]; in the Jiudiantang deposit, the Se contents in cinnabar, stibnite and metacinnabar range from 230 to 3500 ppm, 19 to 38 ppm and 65 ppm, respectively [12]. Additionally, there is very high Se content in the cinnabar from the Yanwuping ore field, with an average content of over 1000 ppm [24]. In the Shangguanxi deposit in the Hunan province, the average Se grade in the ore is 0.31 wt.%, and Se minerals could also be found (e.g., tiemannite with 25.04 wt.% Se [25]). The exposed strata are mainly composed of Precambrian strata, Cambrian to Ordovician

3. Geological Characteristics of Deposit

3.1. Ore Zones and Orebodies

The Wanshan mercury ore field is located in the south of the TFHB. It occurs as a narrow band with a width of 4 km, and the deposits in the area are controlled by the WNW–NW trending secondary fold zone and faults (Figure 1c). The Middle Cambrian Aoxi Formation (E_2a) and the Lower Cambrian Qingxudong Formation (E_1q) are the main host rocks. Most of the Hg mineralization took place in the upper part of the Middle Cambrian Aoxi Formation (E_2a^3) (Figure 1c), which is composed dominantly of dolostones [16].

The occurrence of the orebody is strictly controlled by strata. From bottom to top, the Middle Cambrian comprises 10 members (Figure 2) [26]: (1) the first member (50–179 m thick) comprises predominantly dark-grey to grey thin-bedded limestone; (2) the second member (20 m thick) consists of brecciated dolomite and limestone; (3) the third member (17–60 m thick), which is one of the principal ore-hosting sequences at the Wanshan mercury ore field, is composed predominantly of banded dolomite and argillaceous dolomite; (4) the fourth member (0–22 m thick) contains predominantly breccia metamorphic dolomite; (5) the fifth member (24–70 m thick), which is one of the principal ore-hosting sequences at the Wanshan mercury ore field, is composed of banded dolomite and argillaceous dolomite; (6) the sixth member’s lithology is similar to that of the fourth member; (7–10) the seventh to tenth members consist predominantly of dolostones. Most of the rocks are gray–dark gray due to the enrichment of organic matter.

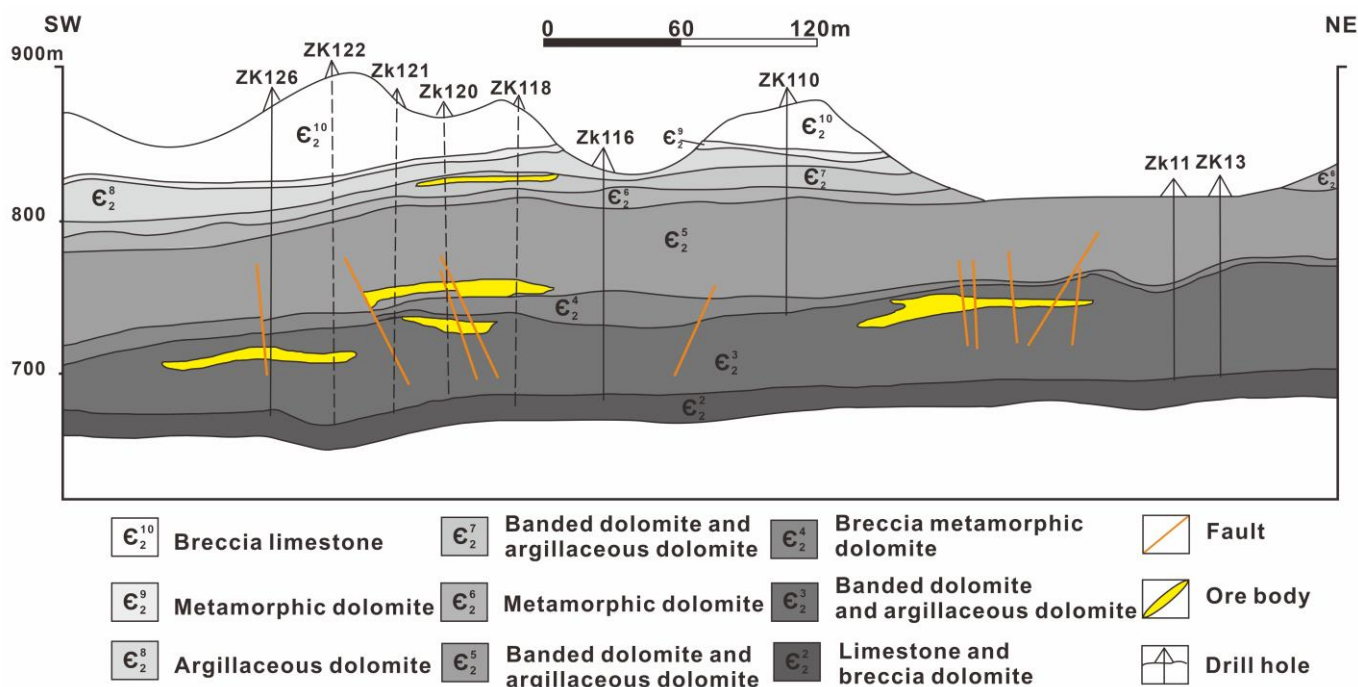


Figure 2. No. 1-1 section of Shanmutong deposit in Wanshan mercury ore field. Modified from Hua [26].

3.2. Ore Mineralogy and Alteration

The three types of ores in our study have distinct characteristics (Figure 3a–d), namely breccia-type Hg ores with cinnabar (Figure 3a,d), irregular vein-type ores (Figure 3b) and cavity-type ores (Figure 3c). Cinnabar mineralization is mostly disseminated and frequently vein-related. The metal mineral assemblage is relatively simple, mainly including cinnabar, pyrite, sphalerite, tiemannite and Se-bearing minerals (e.g., cinnabar, metacinnabar); the gangue minerals are quartz, dolomite, calcite, barite, asphalt, etc., and a large amount of primary asphalt associated with cinnabar [26,27]. Three types of alteration, i.e., silicification, carbonatization and asphaltting, are found in the rocks of the Wanshan ore field [28].

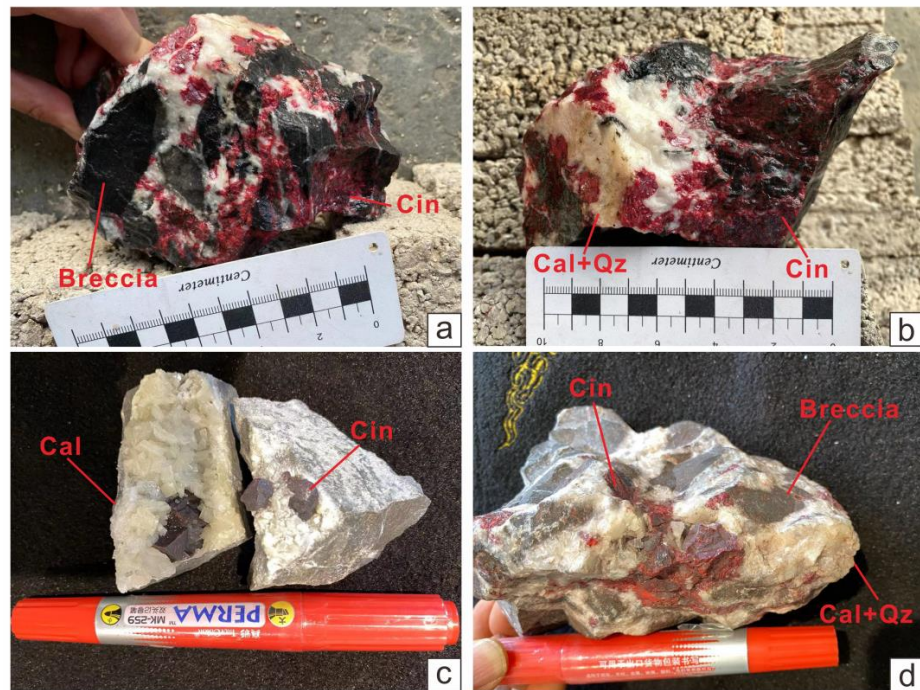


Figure 3. Typical mineral assemblages and textures of the samples of the Wanshan mercury ore field. (a,b) Fine-grain cinnabar fills in a fracture in dolostone; (c) dolostone with its cavity filled by coarse-grain cinnabar and calcite; and (d) brecciated mercury ore. Abbreviations: Cin = cinnabar; Qz = quartz; Cal = calcite.

3.3. Mineralization Stages

Based on a paragenetic sequence, mineral assemblages and textures observed in this study, combined with information from previous studies of the Wanshan mercury ore field [26,29,30], two successive stages of mineralization in the ore field were established: (1) Stage I, selenides–cinnabar–quartz veins filled in silicified rocks, the tiemannite and Se-bearing minerals formed mainly in the stage and (2) Stage II, the widely distributed cinnabar–carbonate stage. The paragenetic sequence in the Wanshan mercury ore field is shown in Figure 4.

Minerals	Stage I	Stage II
Quartz	—————	
Pyrite		—————
Sphalerite	— — — — —	—————
Tiemannite	— — — — —	
Se-bearing metacinnabar	— — — — —	
Cinnabar		—————
Realgar		— — — — —
Stibnite		— — — — —
Calcite		—————

Figure 4. Paragenetic sequence of ore minerals in the Wanshan mercury ore field [26,29,30].

4. Sampling and Analytical Methods

4.1. Sample Collection and Characteristics

Three different types of samples were collected. (1) Altered carbonate rocks at the periphery of the Wanshan mercury ore field and Se-bearing metacinnabar occur in the quartz veins with silicic alteration. In hand specimens, Se-bearing metacinnabar is gray-black with a grain size from 0.5 to 0.8 cm, and it is closely associated with cinnabar (Figure 5a–c). (2) Se-bearing cinnabar (dark red) from dolomite occurs as euhedral crystals hosted by quartz clusters (Figure 5d). (3) Red cinnabar occurs in gray dolomite veins (Figure 5e,f).

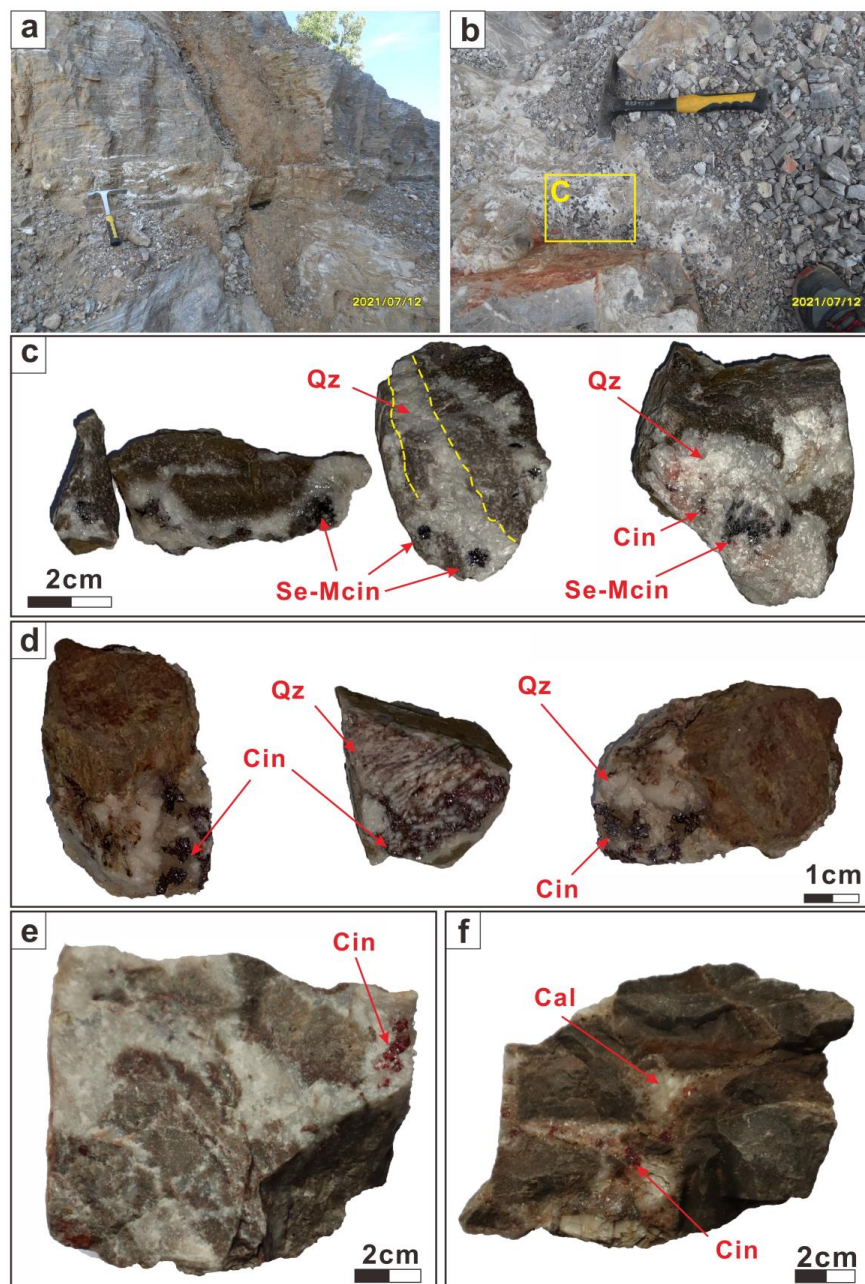


Figure 5. Photographs showing ores and mineral assemblages of Se-bearing metacinnabar and cinnabar in the Wanshan mercury ore field. (a,b) Representative sections with intense silicic alteration; (c) Se-bearing metacinnabar in the quartz veins; (d) Se-bearing cinnabar in the quartz veins; (e) cinnabar–quartz–calcite veins in dolomite; and (f) cinnabar in brecciated mercury ore. Abbreviations: Se-Mcin = Se-bearing metacinnabar; Cin = cinnabar; Qz = quartz; Cal = calcite.

4.2. XRD Analysis

To accurately determine whether the collected black minerals are either Se-bearing metacinnabar or some black iron oxides or Se-dominated minerals (tiemannite), the black mineral and the Se-bearing cinnabar in the quartz veins were selected, washed and crushed step by step. After being picked under a binocular microscope, the samples were ground into powder using agate mortar until there was no obvious granularity. The phase composition was tested and analyzed by XRD at the powder crystal diffraction laboratory, Institute of Science, China University of Geosciences (Beijing). The instrument was SmartLab9KW rotary anode diffractometer (Rigaku, Japan) and the rotary target was a Cu target. The data were collected under the experimental conditions of scanning angle of 3° – 70° and scanning step of 10° /min. Peaks were matched using ICDD pdf in Jade 6.5 software.

4.3. EPMA

In polished sections, ore minerals and textures were observed using standard techniques of reflected-light microscopy. Mineral chemical compositions was determined by EPMA using a JEOL JXA-8230 housed at Hebei Key Laboratory of Earthquake Dynamics, Institute of Disaster Prevention, Langfang, China. The operating conditions were: accelerating voltage of 20 kV, beam current of 20 nA, and an electron beam diameter of 1–5 μm . Standard minerals and metals used for calibration of elemental X-ray intensities were: FeS_2 (Fe and S), Sb_2S_3 (Sb), Bi_2Se_3 (Se), GaAs (As), Co (Co), Cu_2O (Cu), ZnS (Zn), PbS (Pb), and HgS (Hg). The data obtained was ZAF-corrected using proprietary Shimadzu software.

4.4. FESEM

Petrographic analysis was carried out on argon ion milling chips using a Zeiss Supra 55 FESEM under 20-kV accelerating voltage with a working distance of ~ 15 mm. This was done at the FESEM Laboratory, China University of Geosciences (Beijing). To characterize topographic features, a secondary electron imaging detector was used. To reveal compositional differences, an AsB detector was used (backscattered electron image; BSE). Before analysis, samples were coated with ~ 4 nm thick carbon. Semi-quantitative analysis of element concentrations of micrometer-sized spots was carried out using an Oxford energy-dispersive X-ray spectrometer (EDS) connected to the FESEM, operated at 10 kV with a working distance of 8.5 mm.

5. Results

5.1. Microscopic Morphology

The ore minerals in the Wanshan ore field are relatively simple, and mainly comprise Se-bearing metacinnabar and cinnabar, accompanied by sphalerite and a small amount of pyrite. These minerals coexist with quartz and/or calcite grains. Based on the EPMA data, the sphalerite was identified as Hg-bearing sphalerite (Hg-Sp) (see Section 5.3). It occurs mainly as euhedral to subhedral crystals with solid solution separation textures. The Se-bearing metacinnabar (Se-Mcin) occurs as euhedral to subhedral grains with size of 0.2–4 mm and is intergrown with quartz (Figure 6a–i). The reflection color of Se-bearing metacinnabar is gray, with reflectivity lower than the cinnabar, and no bi-reflectance and polychromatism (Figure 6g–i,l,m). The cinnabar is a reflective grayish white with bi-reflectance and obvious internal reflection (red–purple red) (Figure 6g,h,m). There are two types of cinnabar (Cin1-1, Cin1-2) that co-exist with Se-bearing metacinnabar. The Cin1-1 crystal is associated with Se-bearing metacinnabar with clear contact (Figure 6a). It was found that a small part of Se-bearing metacinnabar shows a significant transition to Cin1-2, which grew around the earlier Se-bearing metacinnabar, which is characterized by fractures and pores. Due to the change in crystal volume after transformation, fractures are developed perpendicular to the junction of the two minerals (Figure 6j). The partially inverted Se-bearing metacinnabar contains thin, somewhat flame-like spindly lamellae of cinnabar, which always go to extinction uniformly and in groups (Figure 6k–m). Notably, numerous Hg-sphalerite are formed at the boundary between Se-bearing metacinnabar and

secondary cinnabar, and in newly generated mineral fractures (Figure 6j). In Stage II, the Cin2 is mainly characterized by the development of a solid solution separation structure, minor pyrite exists as mineral inclusions, and Hg-bearing sphalerite occurs as emulsion droplets (2–10 μm) in cinnabar (Figure 6n,p,q).

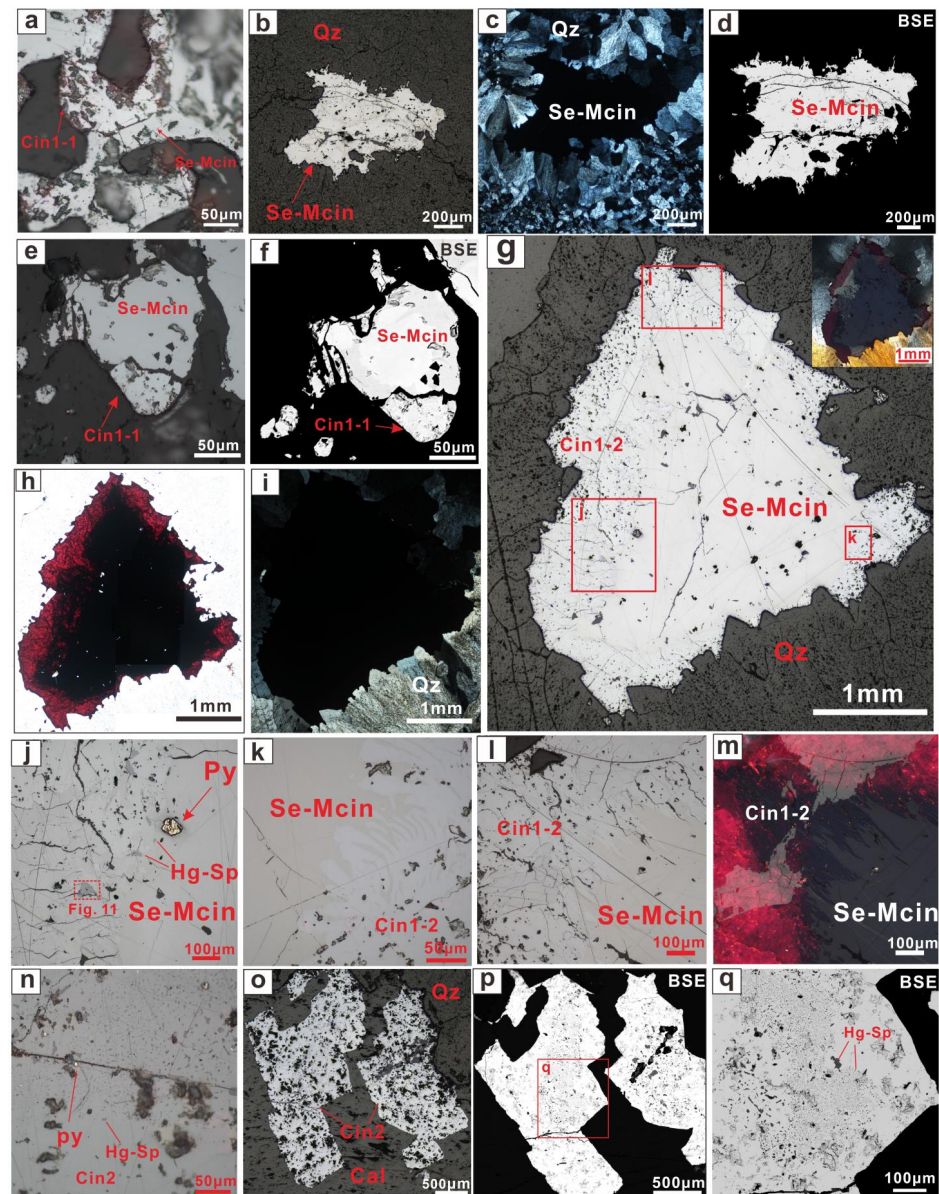


Figure 6. Backscattered electron images and photomicrographs of Se-bearing metacinnabar, cinnabar and sphalerite from the Wanshan mercury ore field. (a) The association of Se-bearing metacinnabar and Se-bearing cinnabar, reflected light; (b–d) Se-bearing metacinnabar in quartz, (a,b) reflected light, (c) cross-polarized light, (d) BSE; (e,f) the association of Se-bearing metacinnabar and Se-bearing cinnabar, (e) reflected light, (f) BSE; (g–i) Se-bearing metacinnabar showing the substantial transition to cinnabar in quartz, (g) reflected light, (h) polarized light, (i) cross-polarized light; (j) the Hg-sphalerite and pyrite hosted in Se-bearing metacinnabar, reflected light; (k–m) flame-like spindly lamellae of cinnabar at the boundary between Se-bearing metacinnabar and secondary cinnabar, (k,i) reflected light, (m) cross-polarized light; (n) emulsion of Hg-bearing sphalerite and pyrite intergrown with cinnabar; (o,p) cinnabar in calcite; (o) reflected light; (p) BSE; and (q) emulsion Hg-bearing sphalerite intergrown with cinnabar, BSE. Abbreviations: Se-Mcin = Se-bearing metacinnabar; Cin1-1 = Se-bearing cinnabar; Cin1-2 = cinnabar transformed from Se-bearing metacinnabar; Cin2 = cinnabar; Py = pyrite; Hg-Sp = Hg-bearing sphalerite; Qz = quartz; Cal = calcite.

5.2. XRD Analysis

Se-bearing metacinnabar and Se-bearing cinnabar from Wanshan mercury ore field were selected for XRD analysis and the XRD patterns results are shown in Figure 7. Compared with the ICDD references, the diffraction peak shown in the XRD pattern of sample 21WS-2-1 is consistent with the PDF 99-0031 (cinnabar), determining its composition as a single cinnabar crystal. However, the diffraction peak shown in the XRD pattern of sample 21WS-2-2 is well consistent with the PDF 22-0729 (metacinnabar) and PDF 99-0031 (cinnabar), indicating that this sample is a mixed phase of Se-bearing cinnabar and Se-bearing metacinnabar. According to the peak strength, Se-bearing metacinnabar is the main component, which is consistent with the results of microscopic observation.

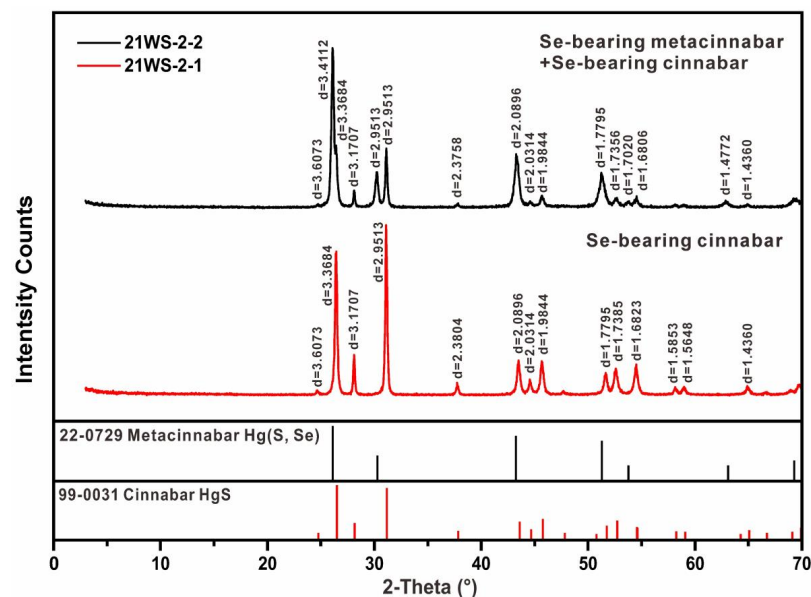


Figure 7. X-ray diffraction patterns of Se-bearing metacinnabar and Se-bearing cinnabar.

5.3. Chemical Compositions of Hg–Se–S and Zn–Hg–S Minerals

Se-bearing metacinnabar, cinnabar and Hg-sphalerite were analyzed by EPMA. Three types of cinnabar were observed: (1) Se-bearing cinnabar (Cin1-1) co-existing with Se-bearing metacinnabar in quartz veins; (2) cinnabar (Cin1-2) transformed from Se-bearing metacinnabar; and (3) cinnabar (Cin2) growing in quartz–calcite veins. The corresponding EPMA data are given in Table 2.

5.3.1. Se-Bearing Metacinnabar (Se-Mcin)

Se-bearing metacinnabar contains 2.79–14.77 wt.% Se (on average, 8.78 wt.%), 6.15–11.82 wt.% S, 77.66–84.01 wt.% Hg (on average, 80.95 wt.%), and 0.18–1.17 wt.% Zn. The average calculated formula of Se-bearing metacinnabar based on EPMA data (Table 2; $n = 21$) is: $\text{Hg}_{1.01}(\text{S}_{0.71}, \text{Se}_{0.29})$.

5.3.2. Se-Bearing Cinnabar (Cin1-1)

Se-bearing cinnabar contains 1.76–3.11 wt.% Se (on average, 2.46 wt.%), 11.65–12.13 wt.% S, and 83.68–85.13 wt.% Hg (on average, 84.55 wt.%). The average calculated formula of Cin1-1 based on EPMA data (Table 2; $n = 4$) is: $\text{Hg}_{1.04}(\text{S}_{0.92}, \text{Se}_{0.08})$.

5.3.3. Cinnabar (Cin1-2)

The cinnabar (Cin1-2) transformed from Se-bearing metacinnabar has 0.69–5.43 wt.% Se (on average, 2.52 wt.%), 10.93–13.08 wt.% S, and 82.13–86.34 wt.% Hg (on average, 84.67 wt.%). The average calculated formula of Cin1-2 based on EPMA data (Table 2; $n = 9$) is: $\text{Hg}_{1.03}(\text{S}_{0.92}, \text{Se}_{0.08})$.

Table 2. EPMA analyses of Hg–Se–S and Zn–Hg–S minerals at Wanshan (wt.%).

No.	1-1	1-2	1-3	1-4	1-5	1-6	1-7	1-8	1-9	1-10	1-11	1-12	2-1	2-2	2-3	3-1	4-1	5-1
Type	Se-Mcin																	
Hg	83.40	81.76	80.09	78.36	78.85	78.30	77.66	79.42	80.73	80.69	79.42	81.93	81.95	82.66	81.08	81.20	82.08	82.46
S	11.09	11.12	8.07	6.79	6.54	6.79	6.15	8.34	8.49	10.07	6.82	9.37	10.44	10.29	9.98	9.59	9.34	11.21
Se	5.20	5.37	10.42	14.06	14.63	13.89	14.77	10.53	10.32	7.09	14.05	8.37	6.42	6.08	6.94	7.71	8.57	5.36
Zn	1.17	1.00	0.25	0.17	0.21	0.08	0.21	0.25	0.28	0.67	0.19	0.41	0.85	0.26	0.66	0.50	0.41	1.05
Total	100.85	99.26	98.82	99.38	100.22	99.05	98.79	98.54	99.82	98.52	100.48	100.07	99.66	99.30	98.67	98.99	100.40	100.08
No.	5-2	6-1	6-2		7-1	8-1	9-1	10-1		11-1	11-2	11-3	11-4	11-5	11-6	11-7	11-8	
Type	Se-Mcin	Se-Mcin	Se-Mcin	n = 21	Cin1-1	Cin1-1	Cin1-1	Cin1-1	n = 4	Cin1-2	n = 8							
Hg	82.35	84.01	81.49	80.95	85.07	83.68	85.13	84.32	84.55	83.77	85.73	85.32	83.55	85.67	86.34	82.13	84.84	84.67
S	10.45	11.82	10.85	9.22	12.13	11.65	12.06	12.08	11.98	11.61	12.18	12.67	12.03	12.59	13.08	10.93	12.18	12.16
Se	6.38	2.79	5.55	8.78	1.76	3.11	2.44	2.51	2.46	3.75	2.23	0.66	2.88	1.81	0.74	5.43	2.66	2.52
Zn	0.73	0.19	0.76	0.49	0.30	0.04	0.28	0.08	0.18	0.16	0.27	0.23	0.07	0.08	0.08	1.05	0.04	0.25
Total	99.90	98.81	98.65	99.44	99.25	98.48	99.91	98.99	99.16	99.29	100.40	98.87	98.53	100.15	100.24	99.54	99.71	99.59
No.	12-1	13-1	14-1	15-1	16-1	16-2	17-1	18-1	19-1		20-1	21-1	22-1	23-1	24-1	25-1		
Type	Cin2	n = 9	Hg-Sp	Hg-Sp	Hg-Sp	Hg-Sp	Hg-Sp	Hg-Sp	n = 6									
Hg	87.22	86.52	86.13	86.48	85.61	85.55	84.68	86.36	85.33	85.99	26.85	33.31	1.50	14.43	17.98	24.77	19.80	
S	13.18	12.79	13.16	13.25	13.09	13.01	14.87	12.93	13.16	13.27	29.42	29.41	32.22	31.79	31.09	30.60	30.76	
Se	0.43	0.66	0.31	0.38	0.31	0.69	0.19	0.21	0.24	0.38	0.38	0.31	bd	bd	0.01	bd	0.23	
Zn	0.26	0.20	0.20	0.24	0.18	0.28	0.23	0.30	0.03	0.21	42.78	38.88	63.28	54.29	51.36	44.03	49.10	
Total	101.08	100.16	99.81	100.35	99.20	99.52	99.97	99.80	98.76	99.85	99.42	101.91	97.00	100.52	100.44	99.41	99.78	

Note: bd = below detection limit (0.01%). Abbreviations: Se-Mcin = Se-bearing metacinnabar; Cin1-1 = Se-bearing cinnabar; Cin1-2 = cinnabar transformed from Se-bearing metacinnabar; Cin2 = cinnabar growing in quartz-calcite veins; Hg-Sp = Hg-bearing sphalerite.

5.3.4. Hg-Bearing Sphalerite (Hg-Sp) and the Cinnabar (Cin2)

The content of Hg in sphalerite ranged from 1.49 to 33.1 wt.% with a mean of 19.80 wt.%. The cinnabar (Cin2) in quartz–calcite veins is almost pure and accompanied only by minute blebs of Hg-bearing sphalerite.

5.3.5. Distribution of Elements in Partially Transformed Se-Bearing Metacinnabar

According to the distribution of elements and mineral assemblage (Figure 8), the partially inverted Se-bearing metacinnabar grains can be subdivided into external cinnabar (Cin1-2) and internal Se-bearing metacinnabar (Se-Mcin), showing systematically lower Se contents and an increasingly higher S from core to rim. The core–rim interface is chemically sharp, and the rim is porous. The internal Se-bearing metacinnabar has the highest Se content, and oscillatory zones with significant differences in Se and S (Figure 8c,e). The distribution of Hg and Zn was relatively homogeneous in Se-bearing metacinnabar (Figure 8b,d). The most interesting feature is revealed by the Se map. The Se-mapping shows a Se concentration gradient from the core to the grain surface (Figure 8d), slowly dropping from 12 wt.% in the core to 7 wt.% at the core–shell boundary, and then quickly dropping to near zero in the shell near the surface. The X-ray element mapping of Hg-bearing sphalerite shows an inhomogeneous Hg and Zn elements distribution with a significant negative correlation, whereas the S distribution is more homogeneous (Figure 8g–i,k–m).

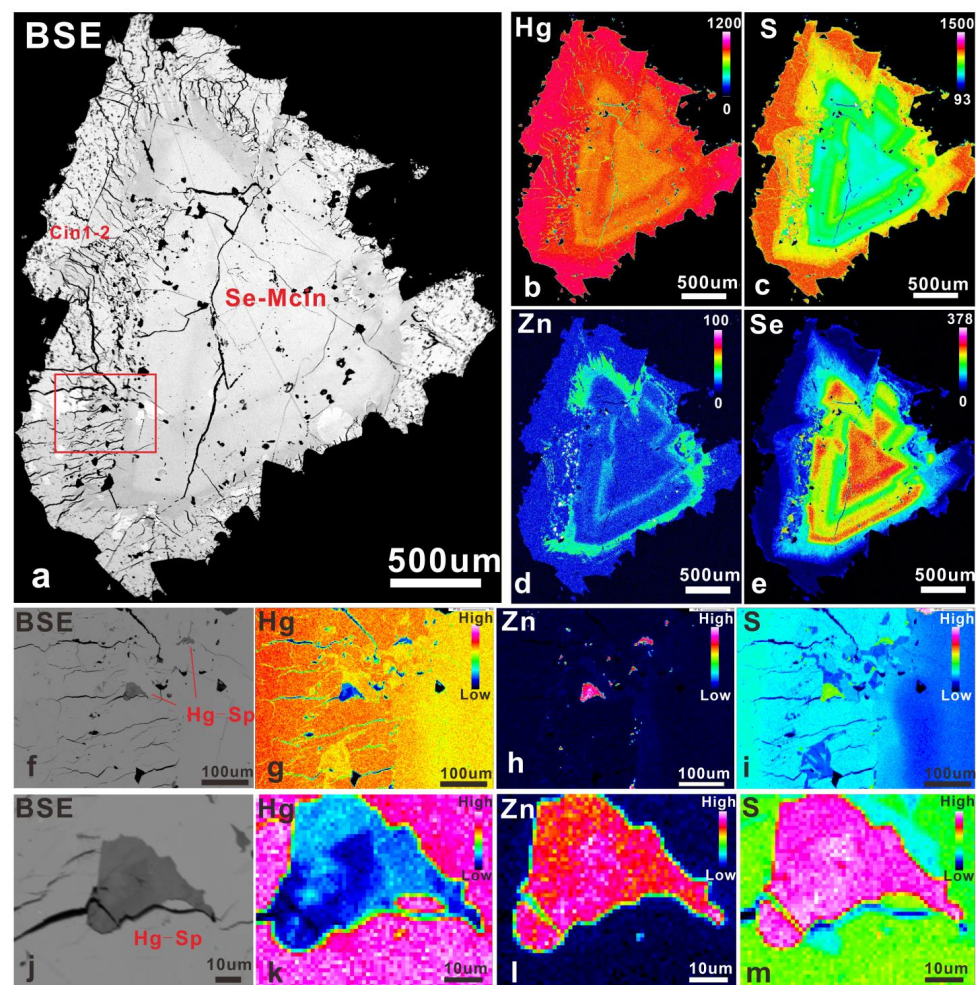


Figure 8. Back-scattered electron (BSE) images (a,f,j); element maps for Hg, S, Zn and Se of the partially inverted Se-bearing metacinnabar (b–e); and element maps for Hg, Zn and S of the Hg-bearing sphalerite (g–i,k–m). Abbreviations: Se-Mcin = Se-bearing metacinnabar; Cin1-2 = cinnabar transformed from Se-bearing metacinnabar; Hg-Sp = Hg-bearing sphalerite.

6. Discussion

6.1. The Hg–Se–S and Zn–Hg–S System Minerals

There are strong correlations between Se and S of Se-bearing metacinnabar (Se-Mcin), cinnabar (Cin1-1, Cin1-2) (Figure 9b), and Hg and Zn of sphalerite (Figure 9c). However, due to the low content of impurity elements, a weaker correlation exists between the Se and S of cinnabar (Cin2) (Figure 9b).

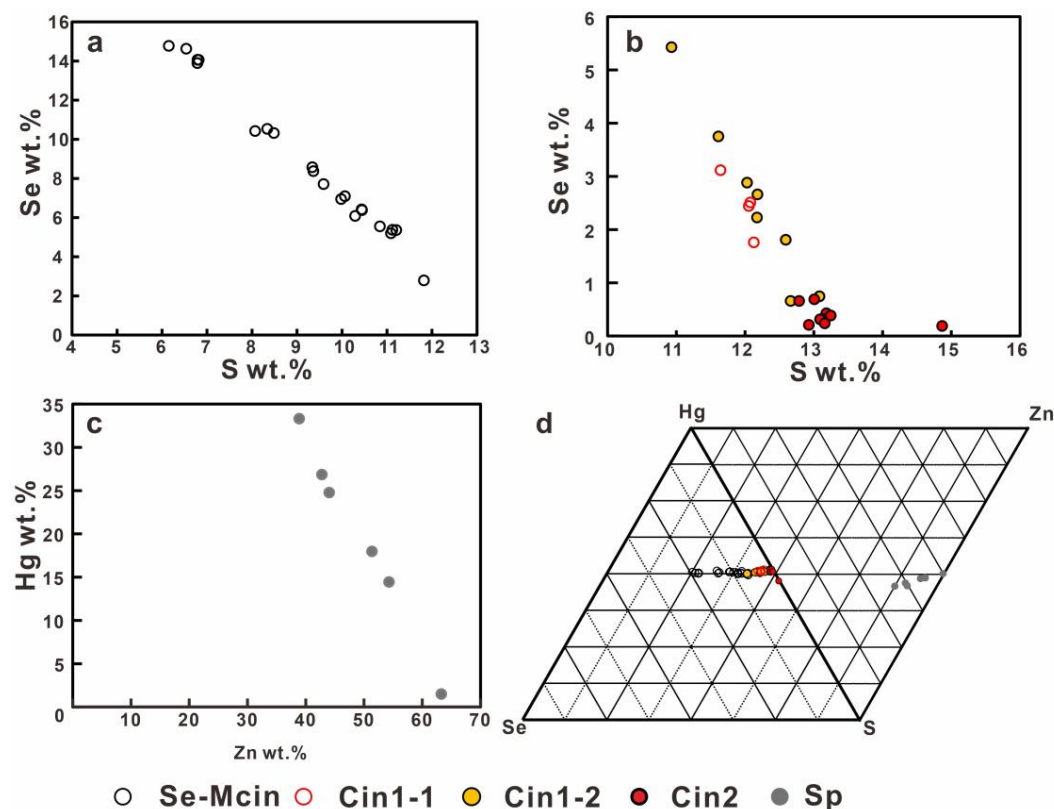


Figure 9. Relationship between Hg, Zn, Se and S in Se-bearing metacinnabar, cinnabar, and sphalerite. (a,b) Se (wt%) vs. S (wt%) plot for the Se-Mcin and cinnabar (Cin1-1, Cin1-2, Cin2); (c) Zn (wt%) vs. Hg (wt%) plot for the Hg-Sp; and (d) quaternion plot of the Hg–Se–S and Zn–Hg–S system minerals. Abbreviations: Se-Mcin = Se-bearing metacinnabar; Cin1-1 = Se-bearing cinnabar; Cin1-2 = cinnabar transformed from Se-bearing metacinnabar; Cin = cinnabar; Sp = sphalerite.

Due to the similar geochemical parameters of Se and S [31], they can form a wide range of isomorphisms. Generally, most of the Se is dispersed in the lattice of sulfides [32], and Se readily forms Se-dominated minerals with cations of high atomic numbers, and with an increase of element affinity, the minerals formed are more stable [33], e.g., stibnite–clausthalite [34,35], galena–kullerudite [36,37], and metacinnabar–tiemannite [13,15,17,38,39]. Figure 9d shows that Se exists as an isomorphous substitution for S in mercury sulfide.

Zn and Hg are IIB elements in the periodic table of elements. Their outer electronic structures are the same, and their geochemical characteristics are similar. β -HgS and sphalerite belong to the same structural type (T_d^2 - $F\bar{4}3m$, $Z = 4$), and Hg-bearing sphalerite has been reported [40–42]. Kremheller [43] also confirmed the complete solid solution of the ZnS–HgS system by hydrothermal method. According to the XAFS study, the mercury in the crystals of Hg-sphalerite and Zn-metacinnabar is in the form of a solid solution, the established nominal oxidation state of mercury is Hg^{2+} [44]. In hydrothermal systems, Hg is a high-vapor pressure element, and it does not instantly switch to the liquid phase at high temperature, forming a Hg-poor sphalerite; but with a temperature decrease, it enters the fluid phase and a Hg-rich sphalerite is formed [13]. According to the S–Hg–Zn diagram,

the changes of Hg and Zn contents in sphalerite were roughly parallel to the Hg–Zn axis (Figure 9d), indicating a Hg^{2+} isomorphous substitution for Zn^{2+} in sphalerite.

Among the Hg–Se–S and Zn–Hg–S system minerals found in the Wanshan ore field, Se-bearing metacinnabar appears as a stable phase, and the admixture of impurity elements plays an important role. Previous authors made a systematic examination of the effect of impurity element admixtures on the stability of metacinnabar under different temperature conditions. Boctor [9] systematically studied the phase relationship of the Hg–Se–S system at different temperatures: a complete solid solution exists between mercury sulfide and mercury selenide at 700 °C; with a temperature decrease, the solid solution series becomes unstable, and a sphalerite-type solid solution coexists with cinnabar near the S endmember at 200 °C. The Hg–Zn–S system has been investigated by Tauson [45] and Din [18]. The T–X diagram at 1 kbar indicates complete miscibility between cubic HgS and ZnS phases at >350 °C (Figure 10), and a high-temperature solid solution with a sphalerite-like structure (the so-called “Hss”) exists [18]. At lower temperatures, the ZnS–HgS diagram splits into two [45]. In the Hg-rich domain (≥ 85 mol% HgS), Hss breaks down into zincian metacinnabar and Zn-free cinnabar; in the Zn-rich domain with 25–84 mol% HgS, two distinct solid solutions (Zn- and Hg-rich), both with a ZnS structure, exist. Finally, cinnabar and Hg-sphalerite comprise the stable low-temperature (<200 °C) assemblage.

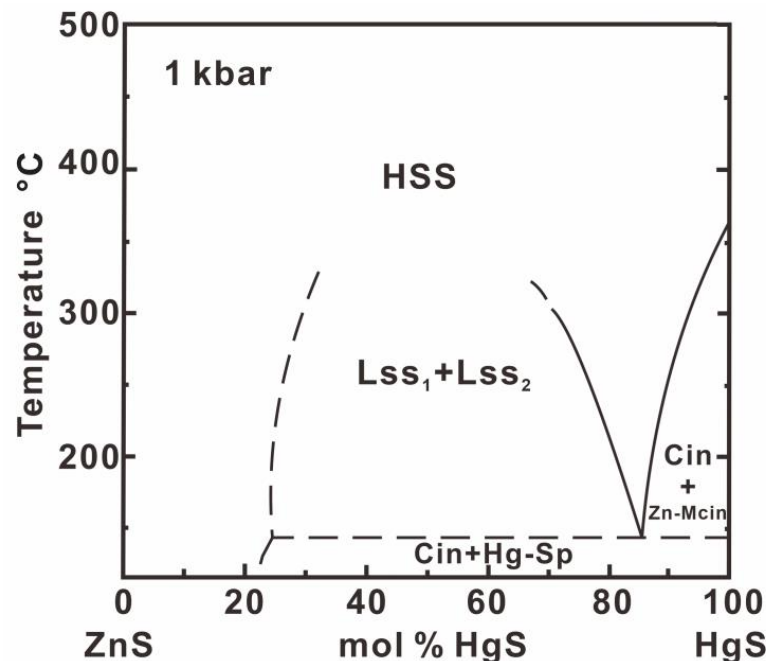


Figure 10. T–X section at 1 kbar pressure of the pseudobinary system HgS–ZnS (modified from Tauson [45]). Abbreviations: Hss = high-temperature (Zn, Hg)S solid solution with sphalerite structure; Lss = low-temperature solid solution; Sp = sphalerite; Zn-Mcin = zincian metacinnabar; Cin = cinnabar; Hg-Sp = Hg-bearing sphalerite.

Under laboratory conditions, as high as 10 mol.% HgSe in the system, the coexistence temperature of metacinnabar and cinnabar was reduced to 248 ± 5 °C [9]. Moreover, about 0.5 wt.% ZnS was sufficient to reduce the transition temperature to 237 ± 3 °C [7]. A small amount of Zn is sufficient to prevent the transformation of metacinnabar into cinnabar, but a higher concentration of Se is needed to produce the same effect. Impurity elements Se and Zn are also found in the Se-bearing metacinnabar collected from this area. Zn contents varied from 0.18 to 1.17 wt.%, with an average value of 0.49 wt.%; Se contents varied from 2.79 to 14.77 wt.%, with an average value of 8.78 wt.%. Therefore, we believe that the reason for the stability of Se-bearing metacinnabar in the Wanshan mercury ore field may be the combined effect of Se and Zn impurity elements.

6.2. Association of Se-Bearing Metacinnabar, Cinnabar and Sphalerite

The cinnabar–sphalerite assemblage usually shows a close relationship with metacinnabar. This has been attributed to the phase transition of metastable metacinnabar, which has been verified by both the natural samples and experiments [5,18,19,46]. Boctor [9] considered the phase transition between cinnabar and metacinnabar as a polymorphic transformation occurring in the dry system, accompanying solid-state diffusion (SSD). In a system that is perfectly dry, SSD often produces continuous composition zones [47]. In our observation, however, the distribution of the Zn element between Se-bearing metacinnabar facies and cinnabar is sharp (Figure 8d), which is not a polymorphic transformation that occurs in a dry system [48]. Additionally, the rim of the metacinnabar is not a completely dry environment, and even very low concentrations of aqueous solutions can substantially increase the rate of solid-state reactions. Therefore, the possibility of SSD is ruled out, and it is considered that polymorphic phase transformations may be caused by coupled dissolution–precipitation reactions (CDR) (e.g., aragonite to calcite, cristobalite to quartz) [49,50].

In our observations, the following features can prove that the phase transition of Se-bearing metacinnabar to cinnabar is accomplished by CDR: (1) Tight spatial coupling of dissolution and precipitation at the interface between the parent and product phases. This coupling preserves the external morphology of the parent phase (Figure 6g–m); (2) sharp parent–product boundary, and no obvious diffusion characteristics in the parent (Figure 8d); (3) the difference in physical properties between metacinnabar and cinnabar, when the replacement reaction involves a volume change between the parent and the product, generates stresses that may eventually lead the mineral to fracture (Figure 6j,i); (4) pathways for fluid infiltration are provided by porosity generation and fracturing, and CDR occurs when unsaturated fluids come into contact with minerals, dissolving the original minerals and creating more stable polymorph (metacinnabar to cinnabar); and (5) some components can be selectively removed from the parent phases by CDR, which could be referred to as “leaching” [50,51]. The reactions between the fluid and the Zn-bearing area in Se-bearing metacinnabar cause the expulsion of the Zn and the precipitation of large amounts of secondary Hg-bearing sphalerite within the replaced zones and the newly generated mineral fractures (Figure 6j). In the presence of a fluid phase (at low temperatures, e.g., <300 °C) and when unsaturated fluids (high sulfur fugacity) come into contact with the parent, the temperature range of mineral formation and $f_{\text{Se}_2}/f_{\text{S}_2}$ determines the final mineral type. According to the reports of Boctor [52] and Sharma [53], the formation temperature of sphalerite can be lower than that of tiemannite, indicating Se removal (to the solution) during the replacement reaction. Overall, we believe that the association of Se-bearing metacinnabar, cinnabar and sphalerite developed in this area is caused by CDR.

Noteworthy, acicular crystals occur within Hg-bearing sphalerite (Figure 11). Bright and grey bands (Figure 11c,d) with a gradual increase in magnification of the BSE image. High resolution line-scan images of bright and grey bands under FESEM reveal a negative relationship between Hg and Zn (Figure 12), which can be caused by one of two possibilities [54]: (1) a special structure; or (2) the presence of two mineral phases. Cook [40] shows a BSE image with “delicate lamellar to dendritic” textures identical to those described here. The acicular crystals within sphalerite have delicate shapes, suggesting a non-turbulent hydrodynamic environment in the vein during growth, and experimental data indicate that the appearance of wurtzite is favored at low temperatures by solutions enriched in cations [55,56]. Wurtzite is metastable and will invert to sphalerite with time [57]. Therefore, cations (Zn) enrichment in solution by “leaching” of CDR at low temperatures, and acicular sphalerite probably inverted from wurtzite by rapid precipitation in such fluid conditions.

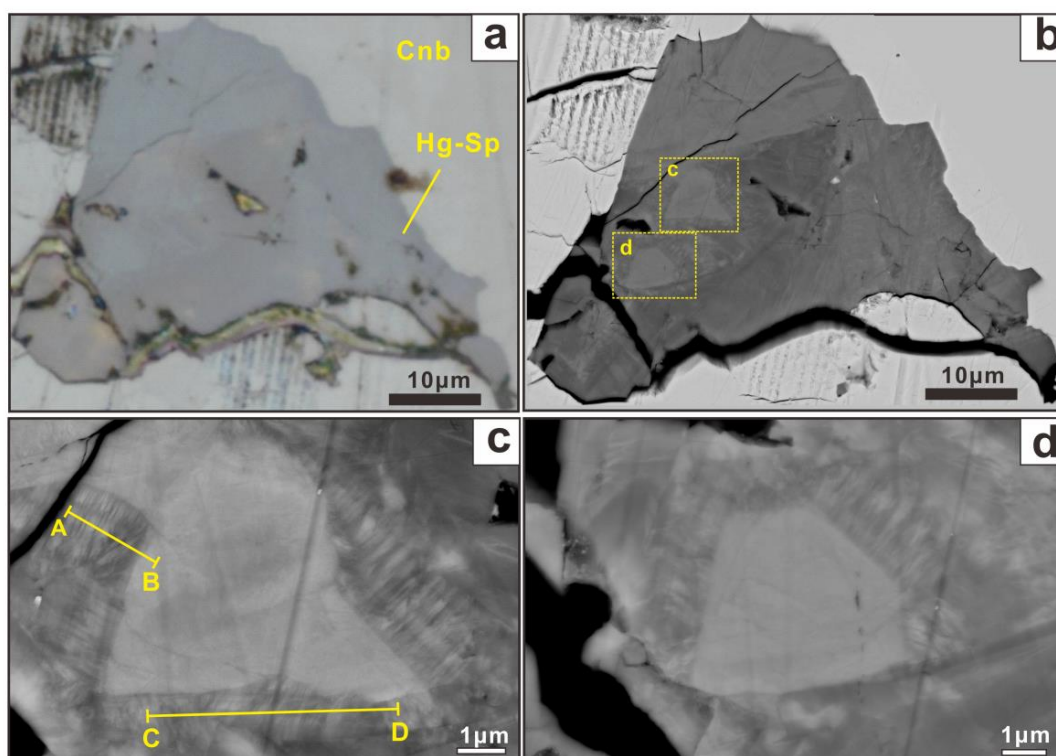


Figure 11. Photomicrographs and SEM images of Hg-bearing sphalerite. (a) Photomicrograph showing an expanded image of Figure 6j local, (b–d). Bright and dark strips are clearly visible with increased magnification of the SEM images. The yellow line represents the micro-zone line scanning analysis area. Abbreviations: Cin = cinnabar; Hg-Sp = Hg-bearing sphalerite.

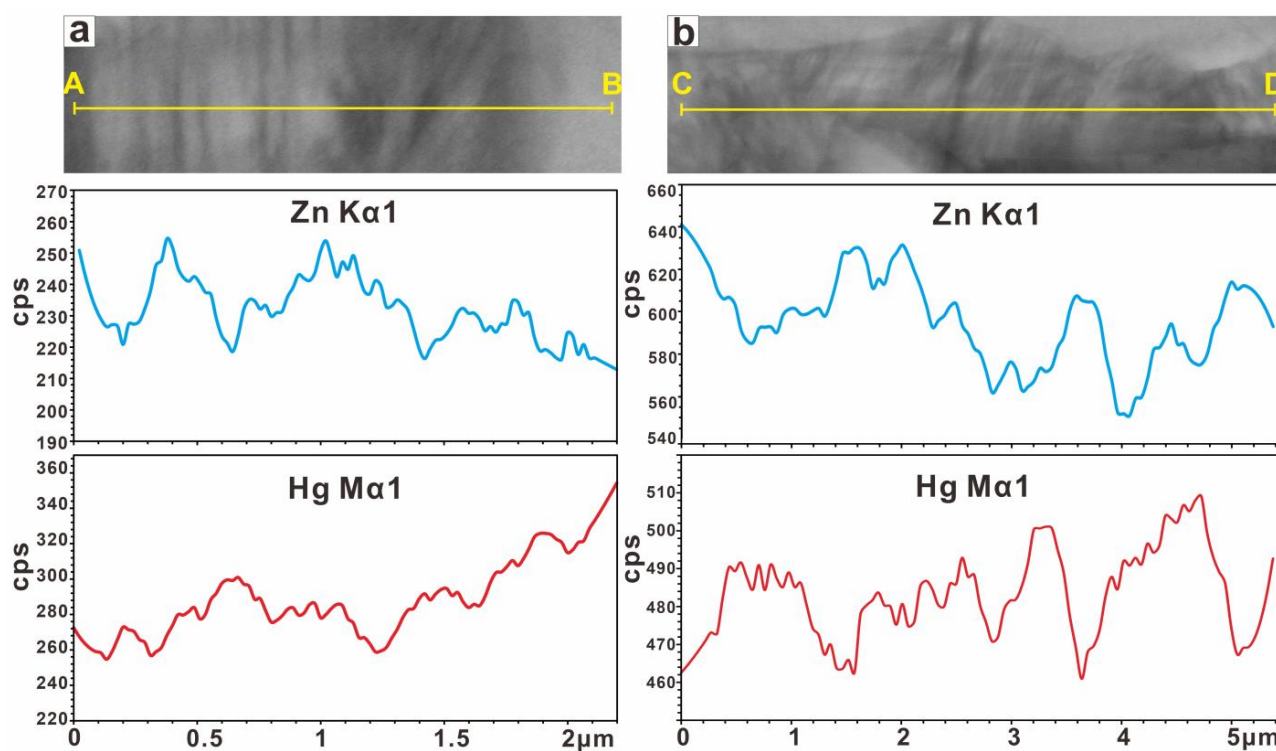


Figure 12. Micro-zone line scanning analysis of the bright and dark bands of Hg-bearing sphalerite. (a,b) The results reveal a negative relationship between Zn and Hg. Note: Bright shades are Hg richer, grey shades are Zn richer.

The oscillatory zones with significant differences in elemental content can be recognized in different Se-bearing metacinnabar samples, which are currently commonly explained by the “intrinsic model” and/or “extrinsic model” [58,59]. Previous studies have shown that mercury ores are often formed under conditions of low temperature and rapid crystallization [60], i.e., the growth of crystals outpaces the diffusion of cations from the liquid into or away from the growing crystals, which leads to the non-equilibrium incorporation of chemical species into the mineral, consistent with the “intrinsic model”. During the crystallization process of Se-bearing metacinnabar (Se-Mcin), the crystallization rate increases with a rapid decrease of temperatures in the early stage, resulting in the uneven distribution of elements in Se-bearing metacinnabar (Se-Mcin) with compositional zonation (Figure 13a). Se-bearing metacinnabar (Se-Mcin) came into contact with saturated fluids, dissolving the Se-bearing metacinnabar to produce more stable minerals (cinnabar, Cin1-2) by CDR (Figure 13b). The product cinnabar (Cin1-2) developed intra-crystalline porosity and fractures, which allowed the fluid to maintain contact with the reaction front (Figure 13c). Similarly, the Zn element in the mineral was continuously brought out of the enrichment, causing the formation of large amounts of Hg-bearing sphalerite at the reaction interface of the two minerals (Figure 13d).

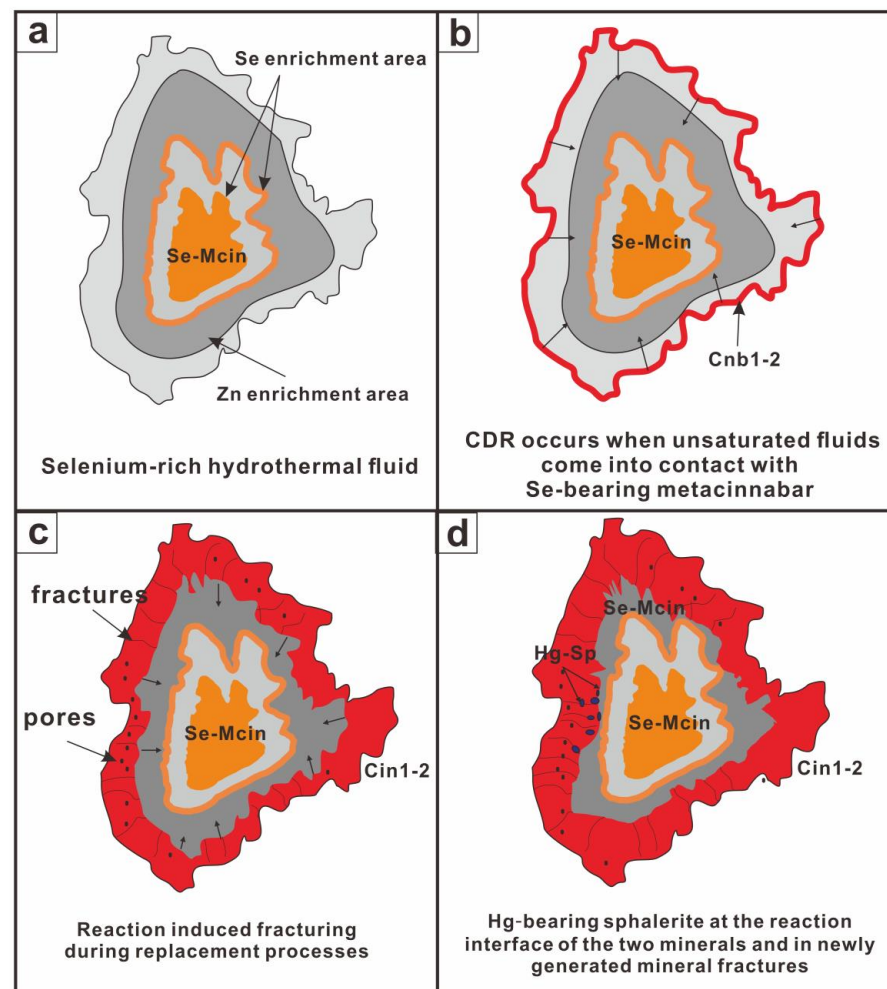
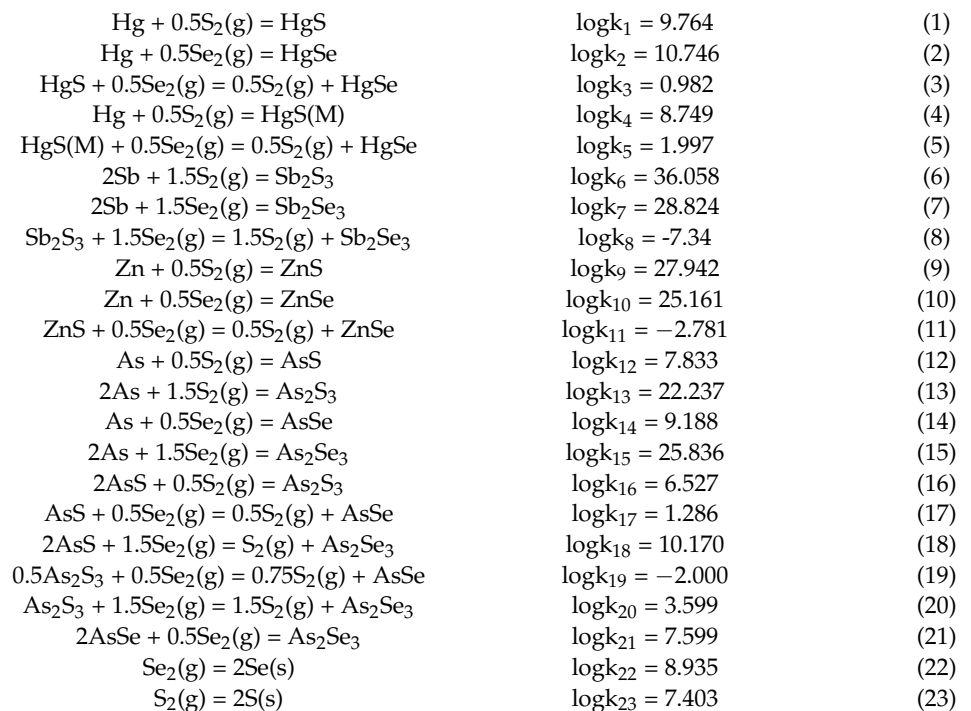


Figure 13. Schematic cartoons illustrating the processes of partial transformation of Se-bearing metacinnabar. (a) The uneven distribution of elements in Se-bearing metacinnabar (Se-Mcin) with compositional zonation. (b) CDR occurs when unsaturated fluids come into contact with Se-bearing metacinnabar. (c) Reaction induced fracturing during replacement processes. (d) Hg-bearing sphalerite at the reaction interface of the two minerals and in newly generated mineral fractures. Abbreviations: Se-Mcin = Se-bearing metacinnabar; Cin1-2 = cinnabar; Hg-Sp = Hg-bearing sphalerite.

6.3. Physicochemical Conditions for the Formation of Se-Bearing Metacinnabar

According to current research that the Hg mineralization of the Xiangqian Hg Belt was formed at a low temperature, with most fluid inclusions having a homogenization temperature of ~ 200 °C [12,26,27]. Based on the detailed microscope observation, the Se-bearing metacinnabar in the Wanshan ore field is closely associated with cinnabar, sphalerite, pyrite, realgar, stibnite, and tiemannite [29,30]. In order to constrain the physicochemical conditions for the formation of Se-bearing metacinnabar, we established the physicochemical phase diagrams according to mineral assemblages and relative reaction relationships. The diagrams were calculated by means of the HSC Chemistry 6.0 software package (chemical equations and thermodynamic data from Simon [61], Xu [62] and HSC Chemistry 6.0 software package), and the following reactions were considered possible mineral deposition processes:



Firstly, Hg-rich and Se-rich hydrothermal fluids form tiemannite, and Se is gradually depleted with the deposition of Se-bearing minerals and/or Se-independent minerals. With a decrease in $f\text{Se}_2/f\text{S}_2$ and the transition from acidic to alkaline ore-forming fluids caused by massive silicification and neutralization of alkaline substances such as CaO, MgO, K₂O, and Na₂O, Se-bearing metacinnabar began to form [29,30]. Based on the observed minerals of the mineral symbiotic association, it is possible to define a range of $\log f\text{S}_2$ between -15.663 and -13.141 , and the absence of HgSe allows us to set an upper limit for $\log f\text{Se}_2 < \log f\text{S}_2 - 3.994$ (the gray area) for the ore-forming fluids at this stage (Figure 14). In the final stage, Se-poor cinnabar formed.

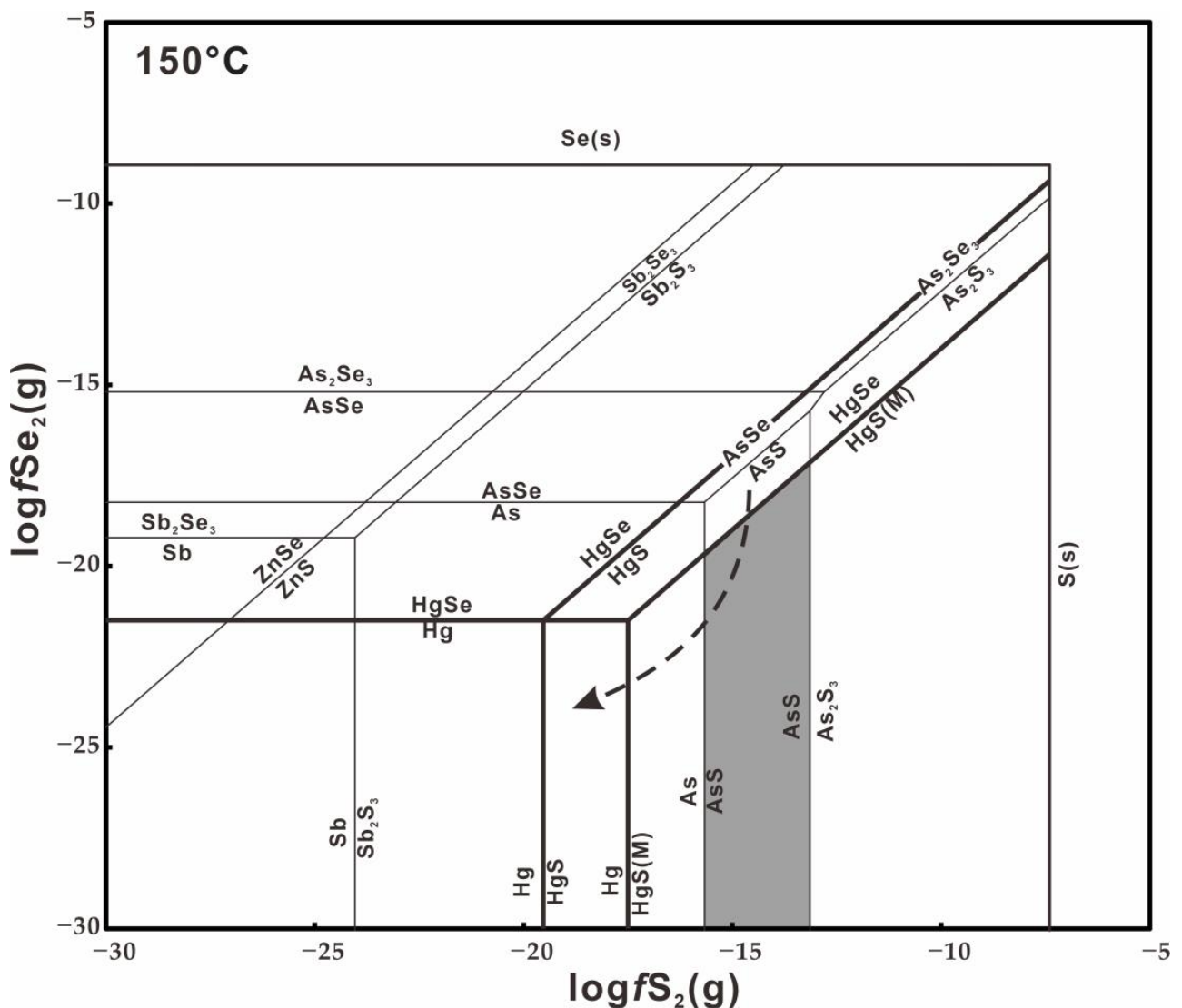


Figure 14. $\log fS_2(g)$ – $\log fSe_2(g)$ diagram showing the relative stability of Se-bearing metacinnabar at 150°C. The gray area represents the fugacity range of $\log fS_2(g)$ and $\log fSe_2(g)$, whereas the dashed curve line represents the evolution trend. Abbreviations: HgS(M) = metacinnabar; HgS = cinnabar; HgSe = tiemannite; AsS = realgar.

7. Conclusions

1. The Se-bearing metacinnabar contains 77.66–84.01 wt.% Hg, 0.18–1.17 wt.% Zn with extensive isomorphic substitution of Se and S (2.79–14.77 wt.% Se, 6.15–11.82 wt.% S), and the presence of impurity elements (Zn, Se) is considered to be the key factor for the stable existence of Se-bearing metacinnabar;
2. The partial transformation of Se-bearing metacinnabar is achieved by coupled dissolution–reprecipitation reactions, which occurred within the Zn-bearing area in Se-bearing metacinnabar, cause the expulsion of the Zn and the precipitation of large amounts of secondary Hg-bearing sphalerite within the replaced zones and the newly generated mineral fractures;
3. The Se-bearing metacinnabar is closely associated with cinnabar, sphalerite, pyrite, realgar, stibnite, quartz and tiemannite and is accompanied by strong silicification, implying that it was formed in acidic conditions and originally precipitated at moderate fSe_2 ($\log fS_2 = -15.663$ to -13.141 and $\log fSe_2 < \log fS_2 - 3.994$ at ~ 150 °C).

Author Contributions: Conceptualization, J.L.; X.W. and J.L. conceived and designed the experiments; X.W. performed the experiments; and analyzed the data; writing—original draft preparation, X.W.; writing—review and editing, E.J.M.C., D.Z., Q.Z., G.W. and B.Z. All authors contributed to the preparation and writing of the manuscript. All authors have read and agreed to the published version of the manuscript.

Funding: This research was financially supported by the Major Research Plan of National Natural Science Foundation of China (Grant No. 92062219), the Records of China’s mineral Geology from China Geological Survey (DD20190379-87), the State Key Program of the National Natural Science Foundation of China (Grant 41730426), the National Key Research and Development Program of China (Grant No. 2018YFC0603704), the 111 Project of the Ministry of Science and Technology (BP0719021), and by MOST Special Fund from the State Key Laboratory of Geological Processes and Mineral Resources, China University of Geosciences.

Data Availability Statement: The data set is presented directly in the present study.

Acknowledgments: We are grateful to Neng Yang for his enthusiastic help during fieldwork. We appreciate Wentan Xu from Institute of Disaster Prevention and Dongjie Tang of the China University of Geosciences (Beijing) for their enormous help with the EPMA and FESEM analyses.

Conflicts of Interest: The authors declare no conflict of interest.

References

1. Hao, A.; Gao, C.; Li, M.; He, C.; Huang, X.; Zhang, D.; Yu, C.; Liu, H.; Ma, Y.; Tian, Y. A study of the electrical properties of HgS under high pressure. *J. Phys. Condens. Matter* **2007**, *19*, 425222. [[CrossRef](#)]
2. Biagioni, C.; Silvia, M.; Pasero, M. New data on metacinnabar from Tuscany (Italy). *Atti della Soc. Toscana di Sci. Nat.* **2017**, *74*, 13–19. [[CrossRef](#)]
3. Biagioni, C.; Orlandi, P. Tiemannite e metacinnabro della miniera Buca della Vena (Alpi Apuane). *Atti della Soc. Toscana di Sci. Nat. Mem.* **2009**, *114*, 13–17.
4. Wang, P. *Systematic Mineralogy*; Geological Publishing House: Beijing, China, 1982; pp. 1–522, (In Chinese with English Abstract).
5. Dickson, F.W.; Tunell, G. The stability relations of cinnabar and metacinnabar. *Am. Miner.* **1959**, *44*, 471–487.
6. Potter, R. The Systematics of Polymorphism in Binary Sulfides, I. Phase Equilibria in the System Mercury Sulfur, II. Polymorphism in Binary Sulfides. Ph.D. Thesis, The Pennsylvania State University, State College, PA, USA, 1973.
7. Potter, R.; Barnes, H. Phase relations in the binary Hg-S. *Eur. J. Miner.* **1978**, *63*, 1143–1152.
8. Ballirano, P.; Botticelli, M.; Maras, A. Thermal behaviour of cinnabar, α -HgS, and the kinetics of the β -HgS(metacinnabar) \rightarrow α -HgS conversion at room temperature. *Eur. J. Miner.* **2013**, *25*, 957–965. [[CrossRef](#)]
9. Boctor, N. The Mercury-Selenium-Sulfur System and Its Geological Implications. Part 1: Phase Relations in the Mercury-Selenium-Sulfur System. Part 2: The Sulfo-selenides and Sulfides of Mercury: Mineralogy and Geochemistry. Ph.D. Thesis, Purdue University, West Lafayette, IN, USA, 1976.
10. Ohmiya, T. Thermal expansion and the phase transformation in mercury sulphide. *J. Appl. Crystallogr.* **1974**, *7*, 396–397. [[CrossRef](#)]
11. Vasil, V.I. New data on the composition of metacinnabar and Hg-sphalerite with an isomorphous Cd admixture. *Russ. Geol. Geophys.* **2011**, *52*, 701–708. [[CrossRef](#)]
12. Bao, Z.; Bao, J. The occurrences of selenium in the western Hunan-eastern Guizhou mercury ore belt. *Miner. Explor.* **1995**, *4*, 30–34. (In Chinese with English abstract)
13. Liu, J.P.; Rong, Y.A.; Zhang, S. Mineralogy of Zn-Hg-S and Hg-Se-S Series Minerals in Carbonate-Hosted Mercury Deposits in Western Hunan, South China. *Minerals* **2017**, *7*, 101. [[CrossRef](#)]
14. Huang, Z. Onofrite in the Dongping mercury deposit, Baojing, Hunan Province. *Acta Miner. Sin.* **1991**, *11*, 274–277. (In Chinese with English abstract)
15. Ye, L.; Cook, N.J.; Liu, T.; Ciobanu, C.L.; Gao, W.; Yang, Y. The Niujiatong Cd-rich zinc deposit, Duyun, Guizhou province, southwest China: Ore genesis and mechanisms of cadmium concentration. *Miner. Deposita* **2012**, *47*, 683–700. [[CrossRef](#)]
16. Bao, Y.; Wan, R.; Bao, Z. Discussion of the mercury mineralization related to the mercury metallogenic belt of Hunan Guizhou province. *Beijing Geol.* **1999**, *2*, 6–13. (In Chinese with English abstract)
17. Wang, J. Mineralization, Geochronology and Geodynamics of the Low-Temperature Epithermal Metallogenic Domain in Southwestern China. Ph.D. Thesis, Graduate University of Chinese Academy of Sciences, Guiyang, China, 2012.
18. Zhang, K. Geological characteristics, ore-controlling regularity and prospecting model of the Southern District of Wanshan mercury deposit. *Miner. Resour. Geol.* **2017**, *31*, 864–868. (In Chinese with English abstract)
19. Zhang, L. *Summary report of supplementary prospecting work in Yanwuping mining area, Tongren County, Guizhou Province*; Guizhou Metallurgical Geology Team No. 1: Tongren, China, 1978. [[CrossRef](#)]
20. Liang, H.; Guan, P.; Chen, M.; Bao, Z.; Bao, J. Metallogenic characteristics and prospecting significance of Hg-Se-Zn deposits at the depth and outside of Jiudiantang Hg deposit, west of Hunan. *Miner. Resour. Geol.* **2016**, *30*, 874–879. (In Chinese with English abstract)

21. Zeng, R. *The Mercury Deposits in China*; Chengdu Geological and Mining Institute, Ministry of Geology and Mining: Chengdu, China, 1983; pp. 27–35. (In Chinese with English abstract)
22. Hua, Y.; Cui, M. *Geology of the Wanshan Mercury Deposits in Guizhou*; Geological Publishing House: Beijing, China, 1995; pp. 1–143. (In Chinese with English abstract)
23. Wu, S. Geological characteristics of the Fanjiashan Hg deposit with a research on its ore-forming rules. *Miner. Resour. Geol.* **2007**, *21*, 618–625. (In Chinese with English abstract)
24. Chen, X.; Li, L. Geological characteristics and sulfur isotopic composition of wanshan mercury deposit in Guizhou and its significance. *Sichuan Nonferrous Met.* **2018**, *4*, 14–17. (In Chinese with English abstract)
25. Wang, H.; Hu, K.; Wu, G.; Chen, H.; Liu, C. *Genesis of Strata-Bound Mercury Deposits in the Border Area between Hunan and Guizhou*; Geological Publishing House: Beijing, China, 1989; pp. 1–366. (In Chinese with English abstract)
26. Liu, Y. *Element Geochemistry*; Sciences Publishing House: Beijing, China, 1984; pp. 1–548. (In Chinese with English abstract)
27. Wen, H.; Xiao, H. A review of selenium minerals. *Acta Petrol. Miner.* **1998**, *27*, 69–74. (In Chinese with English abstract)
28. Liu, J.J.; Zhai, D.G.; Wang, D.Z.; Gao, S.; Yin, C.; Liu, Z.J.; Wang, J.P.; Wang, Y.H.; Zhang, F.F. Classification and mineralization of the Au-(Ag)-Te-Se deposits. *Earth Sci. Front.* **2020**, *27*, 79–98. (In Chinese with English abstract)
29. Liu, J.J.; Zheng, M.H.; Liu, J.M.; Su, W.C. Geochemistry of the La'erma and Qiongmo Au–Se deposits in the western Qinling Mountains, China. *Ore Geol. Rev.* **2000**, *17*, 91–111. [[CrossRef](#)]
30. Owen, N.D.; Ciobanu, C.L.; Cook, N.J.; Slattery, A.; Basak, A. Nanoscale study of clausthalite-bearing symplectites in Cu-Au-(U) ores: Implications for ore genesis. *Miner.* **2018**, *8*, 67. [[CrossRef](#)]
31. Drábek, M.; Vymazalová, A.; Laufek, F. The system Hg-Pd-Se at 400 °C: Phase relations involving tischendorfite and other ternary phases. *Can. Miner.* **2014**, *52*, 763–768. [[CrossRef](#)]
32. Števkó, M.; Sejkora, J.; Dolníček, Z.; Škácha, P. Selenium-Rich Ag–Au Mineralization at the Kremnica Au–Ag Epithermal Deposit, Slovak Republic. *Minerals* **2018**, *8*, 572. [[CrossRef](#)]
33. Cabral, A.R.; van den Kerkhof, A.; Sosa, G.; Nolte, N.; Ließmann, W.; Lehmann, B. Clausthalite (PbSe) and tiemannite (HgSe) from the type locality: New observations and implications for metallogenesis in the Harz Mountains, Germany. *Ore Geol. Rev.* **2018**, *102*, 728–739. [[CrossRef](#)]
34. Marquez-Zavalia, M.F.; Galliski, M.A.; Škácha, P.; Macek, I.; Sejkora, J.; Dolníček, Z. Mineralogy of the Rincon Blanco selenide occurrence, La Rioja, Argentina. *J. Geosci.* **2021**, *66*, 1–14. [[CrossRef](#)]
35. Bao, J. Occurrence characteristics and geological significance of selenium in Xiangxi Mercury Deposit. *Hunan Geol.* **1983**, *2*, 52–57. (In Chinese with English abstract)
36. Chen, D.; Sun, S. Metacinnabar and tiemannite in Hunan-Guizhou (Xiangqian) mercury metallogenic belt. *Acta Petrol. Miner.* **1991**, *10*, 58–62. (In Chinese with English abstract)
37. Cook, N.J.; Ciobanu, C.L.; Pring, A.; Skinner, W.; Shimizu, M.; Danyushevsky, L.; Saini-Eidukat, B.; Melcher, F. Trace and minor elements in sphalerite: A LA-ICPMS study. *Geochim. Cosmochim. Acta* **2009**, *73*, 4761–4791. [[CrossRef](#)]
38. Radosavljević, S.A.; Stojanović, J.N.; Pačevski, A.M. Hg-bearing sphalerite from the Rujevac polymetallic ore deposit, Podrinje Metallogenic District, Serbia: Compositional variations and zoning. *Chem. Erde-Geochem.* **2012**, *72*, 237–244. [[CrossRef](#)]
39. Sokol, E.V.; Kokh, S.N.; Nekipelova, A.V.; Abersteiner, A.; Seryotkin, Y.V.; Ershov, V.V.; Nikitenko, O.A.; Deviatiarova, A.S. Ge-Hg-Rich Sphalerite and Pb, Sb, As, Hg, and Ag Sulfide Assemblages in Mud Volcanoes of Sakhalin Island, Russia: An Insight into Possible Origin. *Minerals* **2021**, *11*, 1186. [[CrossRef](#)]
40. Kremheller, A.; Levine, A.K.; Gashurov, G. Hydrothermal Preparation of Two-Component Solid Solutions from II–VI Compounds. *J. Electrochem. Soc.* **1960**, *107*, 1–27. [[CrossRef](#)]
41. Tonkacheev, D.; Vikentyev, I.; Vymazalova, A.; Merkulova, M.; Trigub, A.; Kovalchuk, E.; Makeyev, A.; Osadchii, V. The chemical state of Hg in synthetic crystals of zinc and mercury sulfides studied by XAFS spectroscopy. *J. Solid State Chem.* **2022**, *305*, 122708. [[CrossRef](#)]
42. Liu, J.J.; Zhai, D.G.; Dai, H.Z.; de Fourestier, J.; Yu, C.; Gu, X.P.; Wang, Y.H.; Yu, H.; Wang, J.P.; Liu, Z.J. Nanoscale characterization of Au₂Te grains from the Sandaowanzi gold deposit, northeast China. *Can. Miner.* **2017**, *55*, 181–194. [[CrossRef](#)]
43. Tauson, V.L.; Ab Ramovih, M.G. A Study of the System ZnS-HgS by the Hydrothermal Method. *Geochem.Int.* **1980**, *17*, 117–128.
44. Din, A.; Benvenuti, M.; Lattanzi, P.; Tanelli, G. Mineral assemblages in the Hg-Zn-(Fe)-S system at Levigliani, Tuscany, Italy. *Eur. J. Miner.* **1995**, *7*, 417–428. [[CrossRef](#)]
45. Boctor, N.; Shieh, Y.; Kullerud, G. Mercury ores from the New Idria Mining District, California: Geochemical and stable isotope studies. *Geochim. Cosmochim. Acta* **1987**, *51*, 1705–1715. [[CrossRef](#)]
46. Velebil, D.; Zacharias, J. Fluid inclusion study of the Horní Luby cinnabar deposit, Saxothuringian Zone, Bohemian Massif: Clues for the metamorphic remobilization of mercury. *J. Geosci.* **2013**, *58*, 283–298. [[CrossRef](#)]
47. Xia, Q.; Liu, J.J.; Li, Y.S.; de Fourestier, J.; Wang, D.Z.; Zhai, D.G.; Yu, X.F.; Lü, X.; Li, X.F. Mineral paragenesis of the Anfangba gold deposit, western Qinling Orogen, China: Implication for coupled dissolution-precipitation reactions and the liquid bismuth collector model. *Ore Geol. Rev.* **2021**, *139*, 104502. [[CrossRef](#)]
48. Sung, Y.-H.; Brugger, J.; Ciobanu, C.; Pring, A.; Skinner, W.; Nugus, M. Invisible gold in arsenian pyrite and arsenopyrite from a multistage Archaean gold deposit: Sunrise Dam, Eastern Goldfields Province, Western Australia. *Miner. Depos.* **2009**, *44*, 765–791. [[CrossRef](#)]

49. Brown, W.; Fyfe, W.; Turner, F. Aragonite in California glaucophane schists, and the kinetics of the aragonite—Calcite transformation. *Can. J. Chem.* **1962**, *3*, 566–582. [[CrossRef](#)]
50. Putnis, A. Mineral Replacement Reactions. *Rev. Miner. Geochem.* **2009**, *70*, 87–124. [[CrossRef](#)]
51. Liu, J.J.; Wang, D.Z.; Zhai, D.G.; Xia, Q.; Zheng, B.; Gao, S.; Zhong, R.C.; Zhao, S.J. Super-enrichment mechanisms of precious metals by low-melting point copper-philic element (LMCE) melts. *Acta Petrol. Sin.* **2021**, *37*, 2629–2656. (In Chinese with English abstract)
52. Boctor, N.; Kullerud, G. Mercury selenide stoichiometry and phase relations in the mercury-selenium system. *J. Solid State Chem.* **1986**, *62*, 177–183. [[CrossRef](#)]
53. Sharma, R.C.; Chang, Y.A. Thermodynamic analysis and phase equilibria calculations for the Zn-Te, Zn-Se and Zn-S systems. *J. Cryst. Growth.* **1988**, *88*, 193–204. [[CrossRef](#)]
54. Beaudoin, G. Acicular sphalerite enriched in Ag, Sb, and Cu embedded within color-banded sphalerite from the Kokanee Range, British Columbia, Canada. *Can. Miner.* **2000**, *38*, 1387–1398. [[CrossRef](#)]
55. Cook, N.J.; Etschmann, B.; Ciobanu, C.L.; Geraki, K.; Howard, D.L.; Williams, T.; Rae, N.; Pring, A.; Chen, G.; Johannessen, B. Distribution and substitution mechanism of Ge in a Ge-(Fe)-bearing sphalerite. *Minerals* **2015**, *5*, 117–132. [[CrossRef](#)]
56. Scott, S.; Barnes, H. Sphalerite-wurtzite equilibria and stoichiometry. *Geochim. Cosmochim. Acta* **1972**, *36*, 1275–1295. [[CrossRef](#)]
57. Shore, M.; Fowler, A.D. Oscillatory zoning in minerals: A common phenomenon. *Can Miner.* **1996**, *34*, 1111–1126.
58. Elardo, S.M.; Shearer, C.K. Magma chamber dynamics recorded by oscillatory zoning in pyroxene and olivine phenocrysts in basaltic lunar meteorite Northwest Africa 032. *Am. Miner.* **2014**, *99*, 355–368. [[CrossRef](#)]
59. Boctor, N.; Brady, J.B. Interdiffusion of S and Se in tiemannite. *Am. Miner.* **1980**, *65*, 797–799.
60. Li, W.; Li, B.; Gu, X.; Huang, Z.; Xiao, D.; Cheng, W.; Chen, C.; Dong, S. Fluid inclusion evidences for the mineralization of the organic fluid in the Yanwuping mercury deposit, Guizhou. *Earth Sci. Front.* **2013**, *20*, 72–81. (In Chinese with English abstract)
61. Simon, G.; Essene, E.J. Phase relations among selenides, sulfides, tellurides, and oxides; I, Thermodynamic properties and calculated equilibria. *Econ. Geol.* **1996**, *91*, 1183–1208. [[CrossRef](#)]
62. Xu, W.; Fan, H.; Hu, F.; Santosh, M.; Yang, K.; Lan, T.; Wen, B. Gold mineralization in the Guilaizhuang deposit, southwestern Shandong Province, China: Insights from phase relations among sulfides, tellurides, selenides and oxides. *Ore Geol. Rev.* **2014**, *56*, 276–291. [[CrossRef](#)]

Disclaimer/Publisher’s Note: The statements, opinions and data contained in all publications are solely those of the individual author(s) and contributor(s) and not of MDPI and/or the editor(s). MDPI and/or the editor(s) disclaim responsibility for any injury to people or property resulting from any ideas, methods, instructions or products referred to in the content.